III

Mapping low frequency carbon radio recombination lines towards Cassiopeia A at 340, 148, 54 and 43 MHz

3.1. Introduction

Molecular hydrogen, the material that fuels star formation, is formed out of atomic hydrogen (e.g., Cazaux & Tielens, 2004). This is clear in the interstellar medium (ISM), where we observe that molecular gas is embedded in atomic hydrogen (e.g., Andersson et al., 1991; Williams & Maddalena, 1996; Moriarty-Schieven et al., 1997; Fukui et al., 2009; Pascucci et al., 2015). Despite the clear association between these two gas compositions, the exact details of what is this atomic envelope are not clear (e.g., Blitz & Williams, 1999; Hollenbach & Tielens, 1999). In order to understand better the relation between mostly molecular dense gas and mostly atomic diffuse gas a larger sample of gas in this transition regime is required, along accurate estimates of its temperature and density.

A way in which we can study the cold atomic gas in the envelopes of molecular clouds is through observations of low frequency ($\nu \lesssim 1$ GHz) carbon radio recombination lines (CRRLs, e.g., Gordon & Sorochenko, 2009). The population of carbon ions recombining to a given principal quantum number, n, is determined by the gas density, temperature and radiation field, as well as the atomic physics involved (e.g., Shaver, 1975; Watson et al., 1980; Salgado et al., 2017a). Thus, we can determine the gas physical conditions by comparing the observed properties of CRRLs at different frequencies with model predictions (e.g., Payne et al., 1989; Kantharia et al., 1998; Oonk et al., 2017). Using this method it has been determined that CRRLs trace cold ($T \sim 100$ K) diffuse gas ($n_{\rm H} \sim 100$ cm^{-3}, e.g., Konovalenko, 1984; Ershov et al., 1987; Sorochenko & Walmsley, 1991; Payne et al., 1994; Kantharia et al., 1998; Roshi & Kantharia, 2011; Oonk et al., 2017) in the Galaxy. These physical conditions are similar to those found from observations of atomic hydrogen associated with molecular clouds, either using self absorption features (HISA e.g., Gibson, 2002; Kavars et al., 2003; Kerton,

2005; Kavars et al., 2005; Moss et al., 2012) or absorption measurements against bright background continuum sources (HICA e.g, Dickey et al., 2009; Stanimirović et al., 2014; Bihr et al., 2015).

Most of our understanding of low frequency CRRLs in the Galaxy comes from studies where the spatial resolution is coarse (e.g., $\theta_{\rm HPBW} \gtrsim 30'$ Anantharamaiah et al., 1988; Erickson et al., 1995; Kantharia & Anantharamaiah, 2001; Roshi et al., 2002). This has hindered a spatially resolved identification of which components of the ISM do low frequency CRRLs preferentially trace, such as the outskirts of HII regions, diffuse CII clouds and/or the envelopes of molecular clouds. A notable exception to this limitation is the line of sight towards the supernova remnant Cassiopeia A (Cas A). Along this line of sight, the bright background continuum (relative to the diffuse synchrotron emission from the Milky Way) enables RRL studies with an effective resolution comparable to the size of Cas A (diameter of $6'$ at 64 MHz, e.g., Oonk et al., 2017). Additionally, the large gas column density in the intervening ISM has allowed a direct detection of CRRLs with a spatial resolution smaller than the size of Cas A (Anantharamaiah et al., 1994; Kantharia et al., 1998; Asgekar et al., 2013). From these observations we know that the optical depth of the CRRLs associated with gas in the Perseus arm increases towards the South of Cas A (Anantharamaiah et al., 1994; Kantharia et al., 1998), peaking against its western hotspot (Asgekar et al., 2013).

Besides low frequency CRRLs, the line of sight towards Cas A has been the target of numerous studies of the ISM (e.g., Davies & Matthews, 1972; Mebold & Hills, 1975; Troland et al., 1985; Bieging & Crutcher, 1986; Wilson et al., 1993; Liszt & Lucas, 1999; De Looze et al., 2017). Given that Cas A is located on the far side of the Perseus arm of the Galaxy (at a distance of 3.4 kpc from the observer Reed et al., 1995), most of the Perseus arm gas lies between the observed and the background source (e.g., Troland et al., 1985). Additionally, the distance between Cas A and the gas in the Perseus arms is large enough that they should be unrelated (Xu et al., 2006; Sorochenko & Smirnov, 2010; Choi et al., 2014; Salas et al., 2017). The spatial distribution of the atomic gas towards Cas A shows that it completely covers the face of Cas A, as revealed by observations of the 21 cm line of HI in absorption against Cas A (e.g., Bieging et al., 1991; Schwarz et al., 1997). However, the saturation of the 21 cm-HI line profiles makes it difficult to identify small scale structure. Observations of other tracers have revealed the presence of gas with a large column density over the southern half of Cas A, with a visual extinction in the range $A_{\rm V} \sim 4$–10 (e.g., Troland et al., 1985; Hwang & Laming, 2012; De Looze et al., 2017). A cartoon illustrating the distribution of the gas relative to Cas A and the observer is shown in Figure 3.1.

The larger optical depth of CRRLs towards the south of Cas A (Anantharamaiah et al., 1994; Kantharia et al., 1998), where CO emission is readily detected, provides evidence, for the association of low frequency CRRLs with cold atomic or diffuse molecular envelopes of molecular clouds (e.g., Andersson et al., 1991). Another argument in favor of this association comes from the gas temperature and density as traced by low frequency CRRLs. Using spatially unresolved observations of CRRLs Oonk et al. (2017) derived a gas electron temperature of 85 K and a density of ~ 280 cm^{-3}, in between those of cold molecular and diffuse atomic gas. A step forward in this direction would be to extend this spatial comparison to the gas physical conditions, which was

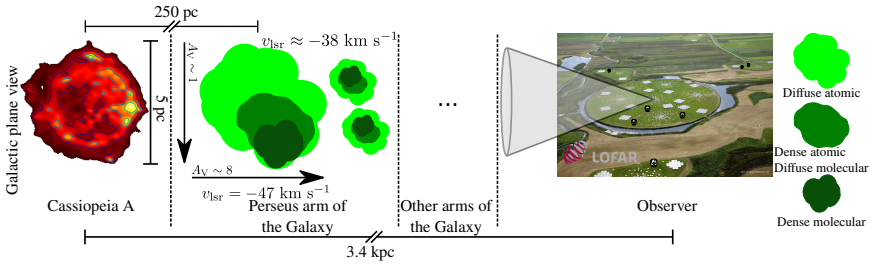

Figure 3.1.: Cartoon depicting the geometry of the studied gas relative to Cassiopeia A and the observer. The gas studied in this work is part of the Perseus arm of the Galaxy and does not show signs of being related to the supernova remnant. The dense molecular gas peaks to the south of Cas A, as shown by continuum observations in the far infrared (De Looze et al., 2017) and CO lines (e.g., Liszt & Lucas, 1999; Kilpatrick et al., 2014). Here we only illustrate the gas over the face of Cas A as our RRL observations do not trace gas outside the face of Cas A.

not possible previously due to the lack of frequency coverage.

In this work we present CRRL emission and absorption cubes centred around the C268α, C357α C494α and C539α lines with a resolution of 70$''$ (1.2 pc at the distance of Cas A). With these cubes we aim to study the relation between the gas traced by low frequency CRRLs and other tracers of cold gas such as cold atomic gas traced by the 21 cm line of HI in absorption and molecular gas as traced by CO lines in the millimetre. We perform this comparison both spatially and in terms of the physical conditions as derived from two sets of lines; one containing the CRRLs and the second the molecular lines.

3.2. Observations & data reduction

Here we describe the data reduction of the low frequency array (LOFAR, van Haarlem et al., 2013) high band antenna (HBA) observations presented in this work, as well as further processing steps applied to the previously published observations used. For the details about the observations collected from the literature we refer the reader to the original works (Table 3.1).

3.2.1. WSRT data

The WSRT data used in this work is the same presented in Oonk et al. (2017). The data reduction steps are the same up to the imaging part. Before imaging, we subtracted the continuum from the calibrated visibilities using *CASA*'s (McMullin et al., 2007) *uvcontsub* (see e.g., van Gorkom & Ekers, 1989; van Langevelde & Cotton, 1990). We use a first order polynomial which is fit to line free channels at both sides of the α lines when possible. After this we imaged the continuum subtracted data using Briggs weighting (Briggs, 1995). We tested using different robust parameters to determine the

Table 3.1.: Selected observations towards Cas A

Line or band	Telescope	Velocity resolution (km s^{-1})	Spatial resolution[c]	Reference
C268α	WSRT	0.6	$70'' \times 70''$ 0°	This work.
C357α	LOFAR HBA	0.7	$18'' \times 18''$ 0°	This work.
C494α	LOFAR LBA	2	$65'' \times 45''$ 100°	Oonk et al. (2017)
C539α	LOFAR LBA	2	$65'' \times 45''$ 100°	Oonk et al. (2017)
HI–21 cm	VLA	0.65	$7'' \times 7''$ 0°	Bieging et al. (1991)
1667 MHz–OH	VLA	1.3	$7'' \times 7''$ 0°	Bieging & Crutcher (1986)
^{13}CO(1–0)[a]	NRAO 12 m	0.13	$56'' \times 56''$ 0°	Liszt & Lucas (1999)
CO(2–1)[b]	SMT	0.3	$33'' \times 33''$ 0°	Kilpatrick et al. (2014)
[CI] $^3P_1$–$^3P_0$	KOSMA	0.63	$54'' \times 54''$ 0°	Mookerjea et al. (2006)
[CII]	Herschel PACS[d]	250	$12'' \times 12''$ 0°	Salas et al. (2017)
A_V			$35'' \times 35''$ 0°	De Looze et al. (2017)

[a] ^{12}CO(2–1) is also available from the same observations.
[b] ^{12}CO and ^{13}CO.
[c] Observing beam major axis, minor axis and position angle.
[d] Herschel is an ESA space observatory with science instruments provided by European-led Principal Investigator consortia and with important participation from NASA.

best trade-off between sensitivity and resolution. Using a robust factor of -1 provided the best angular resolution $\theta \leq 70''$ for most subbands (40 out of the 6×8 subbands). A robust factor of 1 provides a factor of two lower spectral noise with a synthesised beam size of $\theta \leq 100''$ (47/48 subbands). We use the cubes generated with a robust of -1 since we are interested in the spatial structure of the line. After imaging we stack the cubes and apply a bandpass correction in the image plane. The stacked cube has a spatial resolution of $70''$ and contains 40 α RRL transitions[1]. The stacked line profile corresponds to RRLs with an average n of 268. After this we compared the stacked line profile extracted from over the face of Cas A with those presented by Oonk et al. (2017). This comparison showed that the spectra agree within errors.

To study the distribution of the weaker C268α -38 km s^{-1} velocity components we convolve the spectral axis of the cube to increase the signal-to-noise. As convolution kernel we use a boxcar four channels wide. This also produces a cube with a similar velocity resolution as that of the C539α cube (see Table 3.1). In order to allow for a better comparison between the C268α and C539α lines we regrid the spectral axis of the C268α cube to match that of the C539α cube.

Of the CRRL data used in this work, the one coming from the WSRT observations is the one with the coarsest spatial resolution.

3.2.2. LOFAR HBA DATA

Cas A was observed with the LOFAR HBA on December 13, 2015 for four hours (obsid: L415239). This data was taken as part of the LOFAR Cassiopeia A spectral survey (LCASS, PI, J. B. R. Oonk). During the observation all 23 + 14 Dutch stations were used. These observations cover the 132.6–152.3 MHz range with 195.3125 kHz wide spectral windows. The correlator was set up to deliver spectral windows with 512 spectral channels. This results in a channel width of 0.75–0.87 km s^{-1}.

Cygnus A was used as amplitude calibrator at the beginning of the observations (obsid: L415237). Phase and amplitude solutions were derived against Cygnus A and then applied to the Cas A data. After transferring the amplitude and phase from Cygnus A, we self calibrated the Cas A data. We started the self-calibration cycle using a small number of clean iterations and short baselines, then in each repetition of the cycle a larger number of clean iterations, as well as longer baselines, were used. The cut-off in the baseline length started at 2000 lambdas and increased to 12000 lambdas. LOFAR has baselines longer than 12000 lambdas, but we decided to stop at this cut-off because the signal-to-noise ratio drops for higher resolution. After imaging, the cubes were convolved to a common resolution of $18''$. The cubes were then converted to optical depth using $\tau_\nu = I_\nu / I_\nu^{\rm cont} - 1$, where I_ν is the spectrum extracted from the data cubes and $I_\nu^{\rm cont}$ is the continuum determined from a linear fit to line free channels (e.g., Oonk et al., 2014; Salas et al., 2017). Any residual bandpass in the optical depth cubes was corrected in the image plane using an order two polynomial.

After this, the RRL optical depth cubes were stacked. In the frequency range between 132.6 and 152.3 MHz there are 16 α RRLs. From these, we selected four lines which

[1] A line involving a change in principal quantum number of $\Delta n = 1$ is called an α line.

were in spectral windows with low radio frequency interference during the observations. The stacked cube has α RRLs with an averaged principal quantum number $n = 357$.

3.2.3. LOFAR LBA DATA

The data reduction of the LOFAR LBA data is described in Oonk et al. (2017, obsid 40787). For this work we have split the ~ 75 CRRLs present in the 33–57 MHz range into two groups; one group uses the first six CRRLs, which have principal quantum numbers $n = 491, 492, 493, 495, 496, 497$, and another group with the remaining CRRLs (see Table 2 of Oonk et al., 2017 for the complete list). This division is made in order to study the CRRL profile at a lower n number, where the effects of pressure and radiation broadening are less severe and it is easier to differentiate velocity components (e.g., Oonk et al., 2017). The stacked cubes have α RRLs with averaged principal quantum numbers of 494 and 539.

3.2.4. LITERATURE DATA

We complement the spatially resolved LOFAR and WSRT cubes presented in this work with observations from the literature. A summary of the literature observations is presented in Table 3.1. From the literature we have selected the following maps; HI–21 cm (Bieging et al., 1991), the 1667 MHz line of OH (Bieging & Crutcher, 1986), ^{12}CO(2–1) and ^{13}CO(2–1) (Kilpatrick et al., 2014), 492 GHz [CI] Mookerjea et al. (2006), and 158 μm [CII] (Salas et al., 2017). Additionally we include the dust-derived interstellar extinction A_V map of De Looze et al. (2017).

To compare observations with different angular resolutions we convolve the maps to a common resolution of $70''$. We use $70''$ to match the resolution of the WSRT cubes. Two exceptions are the 158 μm [CII] cube and A_V map. We do not convolve the 158 μm [CII] cube since the area covered by each PACS observation is smaller ($45'' \times 45''$) than the target resolution. As for the dust-derived A_V map, we do not convolve because the images used to model the dust emission were analysed at $35''$ resolution (De Looze et al., 2017).

3.3. RESULTS

3.3.1. GLOBAL VELOCITY STRUCTURE

In terms of the line of sight structure, the gas towards Cas A is observed in various ISM tracers in at least four velocity components. One component corresponds to gas in the local Orion spur at velocities close to 0 km s^{-1} (all velocities are referenced with respect to the local standard of rest). The remaining velocity components, and main focus of this work, are associated with the Perseus arm of the Galaxy at velocities of -47, -41 and -36 km s^{-1}. These last two velocity components have been treated as a single velocity component at -38 km s^{-1} in previous CRRL studies because they are difficult to separate (e.g., Payne et al., 1994; Kantharia et al., 1998; Oonk et al.,

2017). Here we use this nomenclature when we are not able to separate the −41 and −36 km s^{-1} velocity components.

To compare the line profiles we averaged the pixels covering the face of Cas A. We define the face of Cas A as a circle of radius 2′.5 centred on $(\alpha, \delta)_{\rm J2000} = (23^{\rm h}23^{\rm m}24^{\rm s}, +58°48'54'')$. The spectra are shown in Figure 3.2. In this Figure we highlight the position of three velocity components, at −47, −41 and −36.5 km s^{-1}. When the spectra shows the presence of these three velocity components, we notice that the velocity of the line peak agrees between different tracers. For the −38 km s^{-1} velocity component we can see that the line profile is a blend of two or more velocity components. This is more readily seen in the line profiles of C268α, ^{12}CO and 1667 MHz–OH, where two velocity components are observed, one close to −41 km s^{-1} and other at −36.5 km s^{-1}.

3.3.2. Channel maps

Here we present spatially resolved C268α and C539α optical depth cubes. The C357α and C494α maps will be shown later (in § 3.3.3), as these show a spatial distribution very similar to that of the C268α and C539α lines (Figures 3.3 and 3.4).

C268α channel maps at velocities around that of the −47 km s^{-1} velocity component are shown in Figure 3.3. These maps show that the gas is predominantly concentrated to the southwest of Cas A. At around −47 km s^{-1} there is emission in an elongated structure running from Cas A's western hotspot to its south. This has been labelled with a white line between the W and S (Figure 3.3). Higher resolution OH observations show that there are three OH clumps over this W-S structure at a velocity $\sim$ −47 km s^{-1} (clumps B, D and E, Bieging & Crutcher, 1986). However, since OH and CRRLs do not trace exactly the same gas, we cannot use this as evidence that the W-S structure is a collection of clumps. With the resolution of the cubes presented in this work it is not possible to distinguish if this is a filament or unresolved clumps.

Channel maps showing velocities corresponding to the Perseus arm features of the C268α and C539α lines are presented in Figure 3.4. Here we use the velocity averaged C268α cube to emphasise features close to −38 km s^{-1}. Emission from the C268α −38 km s^{-1} velocity component is located in the western side of Cas A as well as in the northeast, with a clump close to the centre of Cas A between −43 and −41 km s^{-1}. This central clump is also identified in OH and CO (Bieging & Crutcher, 1986; Wilson et al., 1993).

In the C539α maps we can see similar structures to those seen in the C268α maps, albeit with more detail due to the higher signal-to-noise ratio of the LOFAR data. The W-S structure is visible between −49 and −37 km s^{-1}. The larger extent in velocity is partially due to (radiation or pressure) broadening of the lines at high n (e.g., Salgado et al., 2017b). The spatial distribution of the C539α −38 km s^{-1} velocity component is harder to interpret due to the blending of the Perseus arm velocity components. If we assume that absorption at the more positive velocities is mainly due to the −38 km s^{-1} velocity component, then the absorption close to −33 km s^{-1} should be representative. At this velocity we see that the absorption comes primarily from the east and west of Cas A, like the C268α emission from this velocity component.

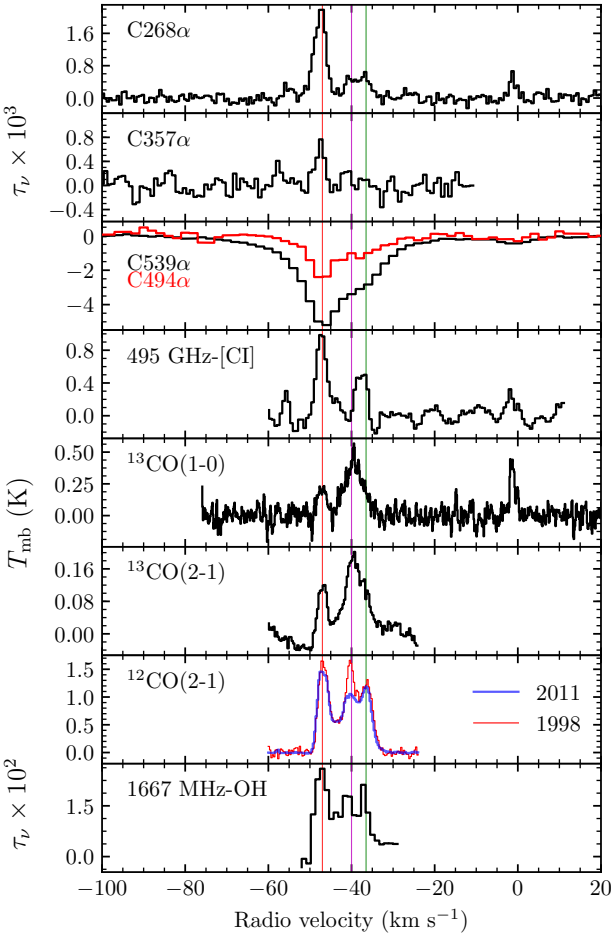

Figure 3.2.: Comparison between the spectra of C268α, C357α, C539α, 492 GHz–[CI], ^{13}CO(1–0), ^{13}CO(2–1), ^{12}CO(2–1) and 1667 MHz–OH. The three CRRLs and the OH line are shown in optical depth units while the [CI] and CO lines in brightness temperature units. The spectra where extracted from an aperture defined by the extent of the 1667 MHz–OH line map. The Perseus arm velocity components at −47, −41 and −36.5 km s^{-1} are shown with *red*, *magenta* and *green* lines respectively. The difference in the 1998 and 2011 ^{12}CO(2–1) line profiles is due to the different choice of off-source position.

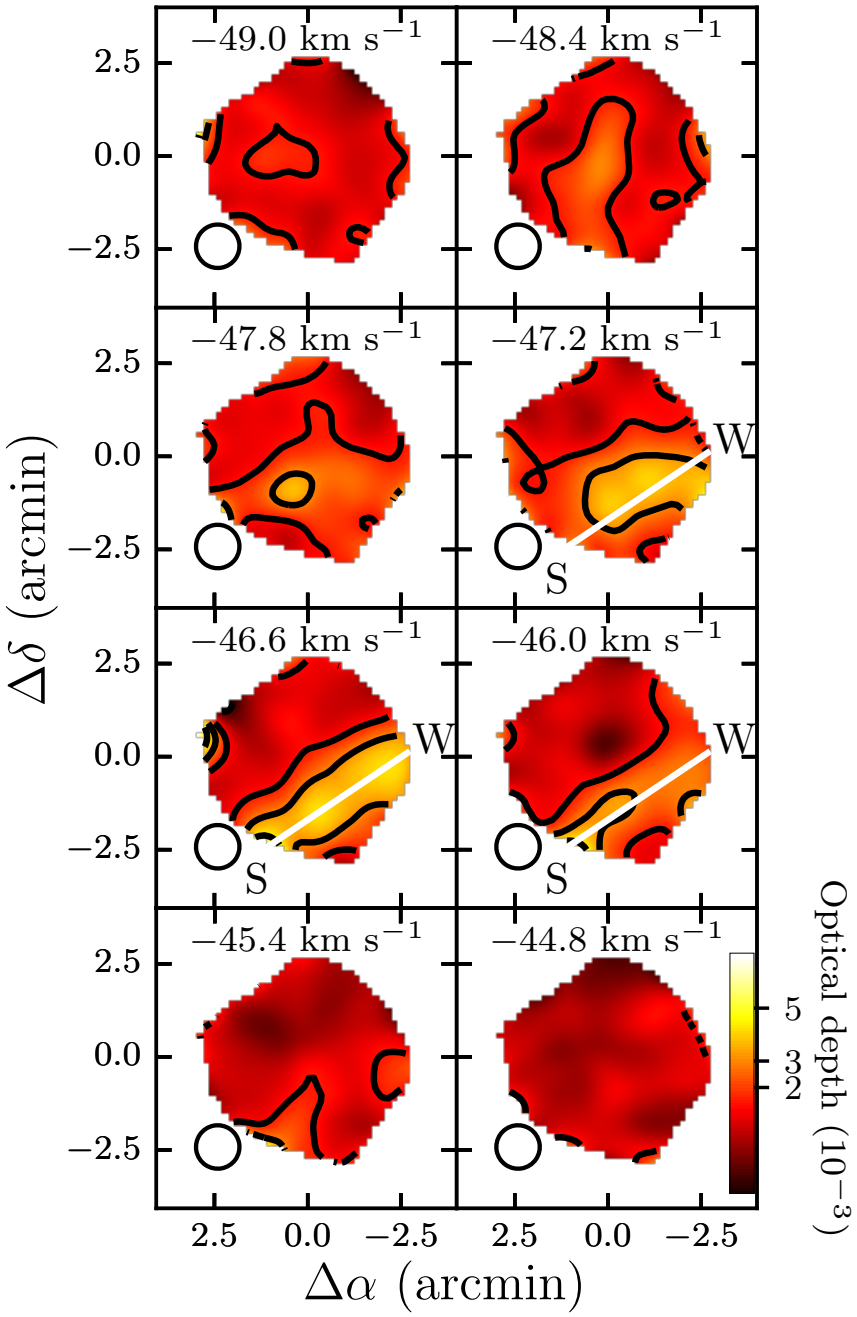

Figure 3.3.: C268α emission around -47 km s^{-1} channel maps. These maps have a spatial resolution of 70″, shown in the lower left corner of each panel. The contours start at 3σ, with $\sigma = 6 \times 10^{-4}$, and continue at values of 4σ, 5σ and 6σ. The white line marks the location of an elongated structure with a W-S orientation.

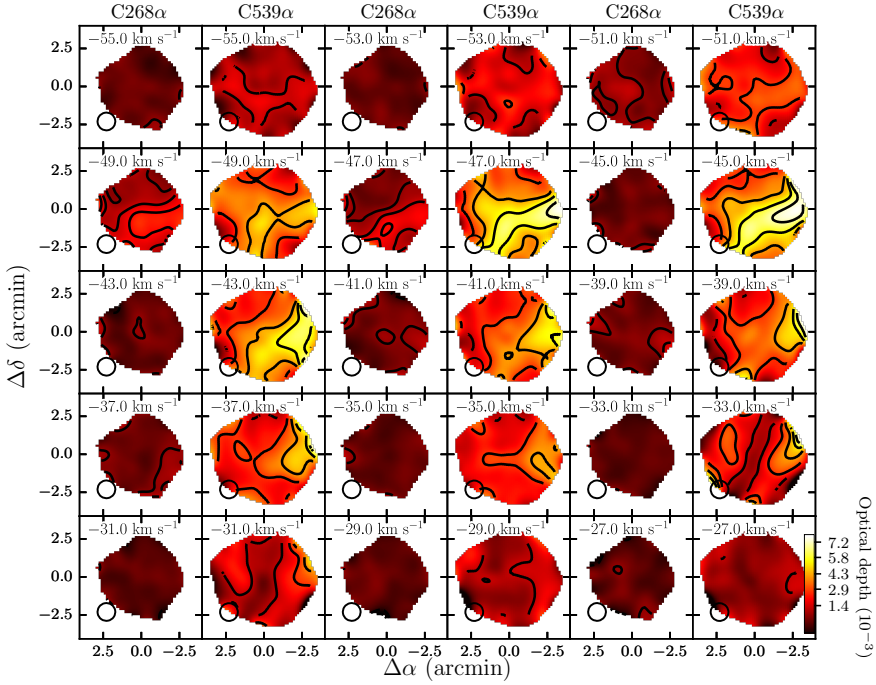

Figure 3.4.: C268α emission and C539α absorption channel maps. The spectral axis of the C268α cube was convolved to a 2.4 km s^{-1} velocity resolution and reggrided to match the spectral axis of the C539α cube. The colour scale is the same for both C268α emission and C539α absorption. The contours start at 3σ with $\sigma = 2.5 \times 10^{-4}$ for C268α and $\sigma = 4.8 \times 10^{-4}$ for C539α. The 70″ resolution of the channel maps is shown in the bottom left corner of each map.

3.3.3. CRRL PROPERTIES

The properties of low frequency CRRLs can be used to determine the gas electron density, temperature and pressure. These properties imprint their signature in the line integrated optical depth as a function of principal quantum number n (e.g. Shaver, 1975; Salgado et al., 2017a). Additionally, the change in line width with n, caused by radiation and pressure broadening, also provides information about the gas properties (e.g. Shaver, 1975; Salgado et al., 2017a).

To determine the line properties over the face of Cas A on a pixel-by-pixel basis we fit the line profiles and construct moment maps. In order to fit the line profiles we first determine where the lines are detected by using the moment masking method as refined by Dame (2011). In this method the data cube is smoothed to a resolution which is two times the original cube resolution in the spatial and spectral directions. Using the smoothed cube we search for significant detections by requiring that the signal-to-noise ratio is above some threshold level. For each pixel/channel which shows a significant detection we also set the neighbouring pixels which are inside the convolution kernel as detections. Then we fit the line profile only in those regions where there are significant detections.

To determine an optimum threshold level we tested using synthetic data cubes. In this test we varied the threshold level between one and ten times the noise in the synthetic data cube and compared the recovered moment 0 with the known input. This test shows that if we use a threshold of three times the noise in the smoothed cube, then the line properties can be recovered with no significant deviation from the input data. For these observations this means that for the higher signal-to-noise line at -47 km s^{-1} we should recover most of the line structure. However, for the weaker velocity component at -38 km s^{-1}, we are likely to recover only the brightest regions.

To fit the RRLs with principal quantum number 268 we use Gaussian line profiles. We fit up to three CRRLs close to -47 km s^{-1}, -38 km s^{-1} and 0 km s^{-1}. Once we have the line properties from the $n = 268$ CRRLs, we use their second and third moments to guide the fit for the higher n lines. In the case of the $n = 357$ lines this is necessary given the lower signal-to-noise ratio. For the $n = 494$ and 539 lines this is done to guide the separation of the blended line profiles. This relies on the assumption that the CRRLs at different frequencies will trace gas with similar properties. Studies which cover a larger frequency range than the one studied here show that the line properties can be accurately modelled by a single set of gas properties (Oonk et al., 2017). With this the line centroid should be the same for different n lines, and for $n \leq 500$ the line profile is dominated by the gas thermal motion (Salas et al., 2017), which does not depend on frequency.

To fit the C357α lines we use two Gaussian profiles, one for the -47 km s^{-1} velocity component and one for -38 km s^{-1}. When fitting we fix the line centroid and line width to those of the C268α line. This leaves the line amplitude as the only free parameter.

To fit the C494α and C539α lines we use two Voigt profiles, one for the -47 km s^{-1} velocity component and one for -38 km s^{-1}. When fitting we fix the line centroid and the Doppler core of the line profiles to those of the C268α lines. This leaves the amplitude and Lorentz width as free parameters. When there is no significant C268α

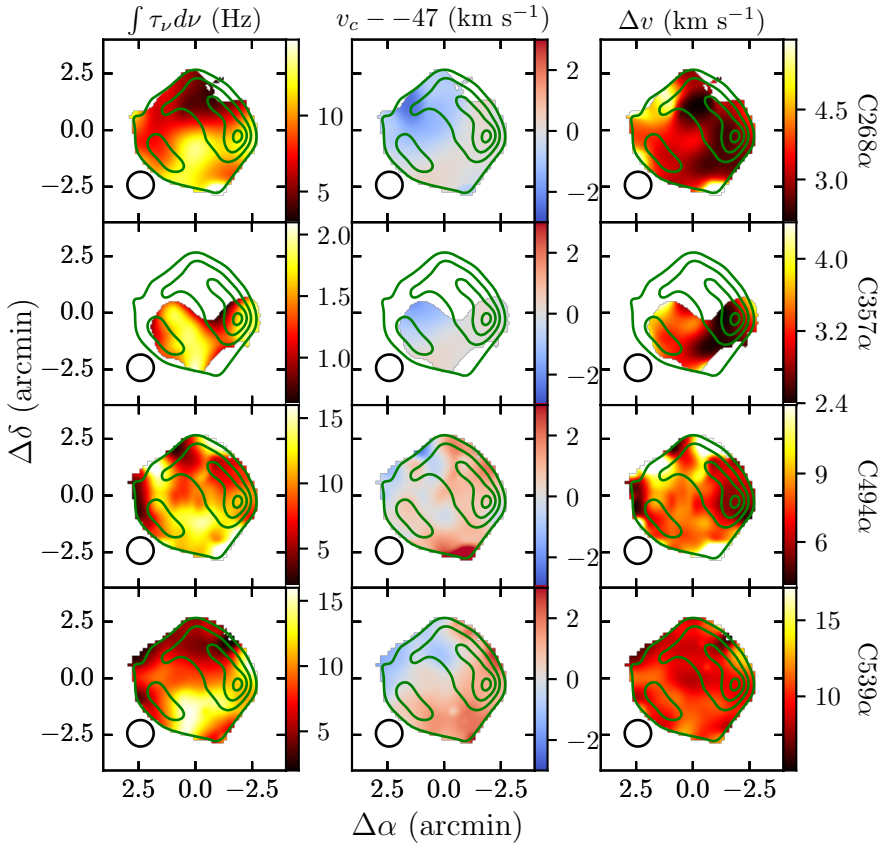

Figure 3.5.: Moment maps for the CRRLs at −47 km s^{-1}. The *top row* shows the moment maps for the C268α line, the *upper middle row* for the C357α line, the *lower middle row* for the C494α line and the *bottom row* for the C539α line. The *left column* shows the integrated optical depth, the *middle column* the velocity centroid of the line with respect to −47 km s^{-1} and the *right column* the full width at half maximum of the line. The *green contours* show the 345 MHz continuum from Cas A at 51″ × 45″ resolution. The 70″ resolution of the moment maps is shown in the bottom left corner of each map. At the edges of Cas A the signal-to-noise ratios are lower due to the fainter continuum.

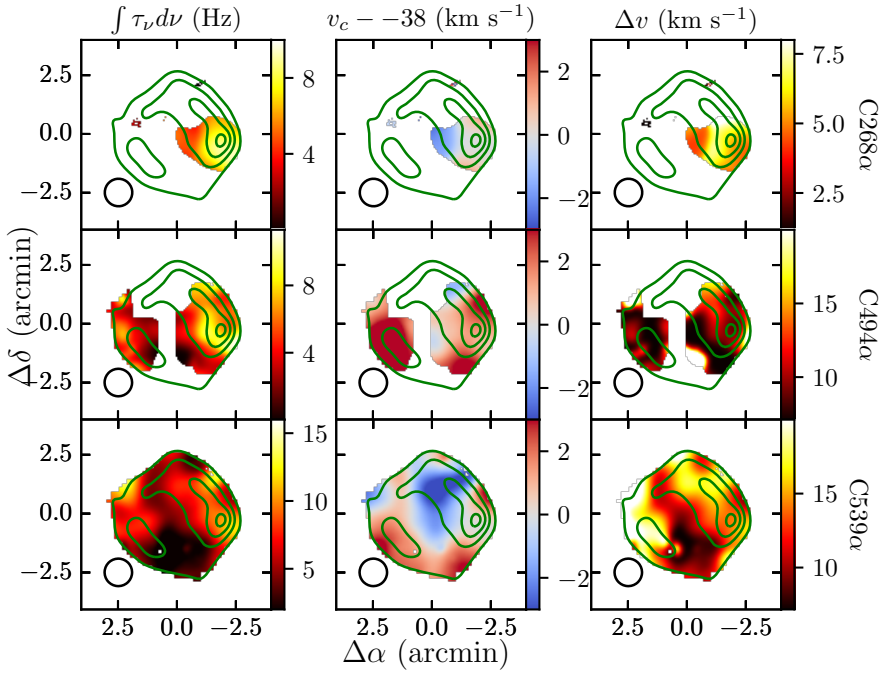

Figure 3.6.: Moment maps for the CRRLs at -38 km s^{-1}. The *top row* shows the moment maps for the C268α line, the *middle row* for the C494α line and the *bottom row* for the C539α line. The *left column* shows the integrated optical depth, the *middle column* the velocity centroid of the line with respect to -38 km s^{-1} and the *right column* the full width at half maximum of the line. Here we do not show the C357α line moments as they are similar to those of the C268α line. The *green contours* show the 345 MHz continuum from Cas A at $51'' \times 45''$ resolution. The $70''$ resolution of the moment maps is shown in the bottom left corner of each map. At the edges of Cas A the signal-to-noise ratios are lower due to the fainter continuum.

line emission we adopt the median values from the C268α moments as initial guesses for the line parameters, but we allow them to vary. This is mostly the case for the line at -38 km s^{-1}.

The moment maps for the $n = 268$ RRL at -47 km s^{-1} are shown in the top row of Figure 3.5. Here we see that emission from the -47 km s^{-1} velocity component extends almost all over the face of Cas A, with a lower integrated optical depth to the north of the remnant. The moment 0, or velocity integrated optical depth, map for the -47 km s^{-1} velocity component shows that most of the emission comes from the W-S structure. The moment 1, or optical depth weighted velocity centroid, map shows that over the W-S structure the velocity remains constant. The moment 2, or full width at half maximum, map shows that the line is narrow in the West and broadens to the East of Cas A. Towards the North-east of Cas A the -47 km s^{-1} C268α line is broader by a factor of ~ 2 with respect to the W-S structure. The CRRL at 0 km s^{-1} is not displayed because at $70''$ resolution the signal-to-noise ratio is lower than three in individual pixels.

The moment maps for the C357α -47 km s^{-1} velocity component are shown in the middle panels of Figure 3.5. These show that the velocity integrated optical depth of the -47 km s^{-1} velocity component is larger in the W-S structure, similar to that observed in the C268α line.

The moment maps for the C539α line at -47 km s^{-1} are shown in the bottom panels of Figure 3.5. These show that most of the C539α absorption from the -47 km s^{-1} velocity component comes from the W-S structure, in accordance with the lower n lines. The moment 2 maps suggests that the -47 km s^{-1} velocity component is broader towards the south-east of Cas A, however the line width is consistent with a constant value over the face of Cas A.

The moment maps for the C268α and C539α -38 km s^{-1} velocity component are shown in Figure 3.6. The C268α line is only detected towards the western hotspot of Cas A. In contrast, the C539α line is detected almost all over the face of Cas A. Both maps show that the peak integrated optical depth is located towards the western hotspot of Cas A. For the C357α line at -38 km s^{-1} the spatial distribution is similar to that of the C268α at the same velocity, a patch $\sim 0.4'$ towards the south of the western hotspot of Cas A.

The moment 2 maps for the -38 km s^{-1} component shows that the line is broader towards the northern half of Cas A, with the broadest line towards the east. The minimum line broadening is observed towards the centre and south of Cas A. This resembles the ridge of CRRL absorption that passes through the centre of Cas A between -33 and -31 km s^{-1} (Figure 3.4).

3.3.4. Physical conditions from CRRLs

The change in the CRRL profile as a function of principal quantum number has the signature of the gas physical conditions imprinted on it (Shaver, 1975; Salgado et al., 2017a). The gas properties which can be determined using CRRLs are its electron density $n_{\rm e}$, electron temperature $T_{\rm e}$ and the intensity at 100 MHz of the radiation field the carbon atoms are immersed in, $T_{r,100}$.

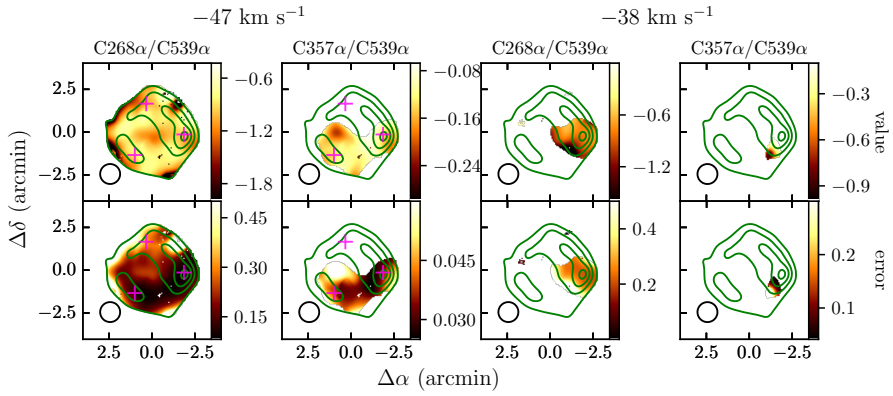

Figure 3.7.: Ratios between different CRRLs at different velocities. The ratios shown are the R_{539}^{268} =C268α/C539α and R_{539}^{357} =C357α/C539α line ratios. The *top panels* show the ratio value and the *bottom panels* the error on the ratio. The *text on top of each column* indicates which ratio is shown in the corresponding column, and a *text label* on the top of the Figure shows the velocity component. The ratios show only regions where both lines involved have been detected with a signal-to-noise ratio larger than three. The *pink crosses* in the top panel show the regions used in Figure 3.8. The 70″ resolution of these maps is shown in the bottom left corner of each map.

To determine the CRRL properties we use the models of Salgado et al. (2017a). To solve the level population problem we assume that collisions with atomic hydrogen and electrons set the relative population of carbon ions in the $^2P_{1/2}$ and $^2P_{3/2}$ states. For the collisional rates we adopt the values of Tielens & Hollenbach (1985) for collisions with hydrogen and those of Hayes & Nussbaumer (1984) for collisions with electrons. We adopt electron and carbon abundances of 3×10^{-4} while solving the level population problem. However, when converting to per hydrogen atom quantities, we adopt electron and carbon abundances of 1.5×10^{-4}. The effect of these assumptions is small ($\sim$ 10%), and will be discussed later. For the ℓ-changing collisional rates we use the semi-classical formulation of Vrinceanu et al. (2012) incorporated into the Salgado et al. (2017a) models. Additionally, when solving the level population problem, a radiation field with a power law shape is included. This radiation field has a spectral index of −2.6, similar to the observed spectral index of Galactic synchrotron emission (e.g., de Oliveira-Costa et al., 2008; Zheng et al., 2016), and its intensity is defined at 100 MHz by $T_{r,100}$ (Shaver, 1975; Salgado et al., 2017a).

In order to model the gas properties we assume that the radiation field the gas is immersed in is constant. Since we are studying gas on scales of $\lesssim$ 1 pc and the gas is at a distance of $\gtrsim$ 220 pc from Cas A (e.g., Kantharia et al., 1998; Salas et al., 2017), the possible contribution of Cas A to the radiation field (Stepkin et al., 2007) will change by a negligible amount over the observed structure. Additionally, there are no other known strong, low-frequency, discrete radiation sources in the field. Considering this, it seems reasonable to assume that the gas is immersed in a constant radiation field.

Table 3.2.: Grid of CRRL models

Parameter	Notation	Value	Step
Electron density	$n_{\rm e}$	0.01–0.1 cm^{-3}	0.005 cm^{-3}
Electron temperature	$T_{\rm e}$	10–400 K	5 K
Radiation field at 100 MHz	$T_{\rm r,100}$	800–2000 K and 1400 K	400 K

Following the results of Oonk et al. (2017) we adopt $T_{r,100} = 1400$ K.

Given the C268α, C357α, C494α and C539α velocity integrated optical depths we explore how these can be used to constrain the gas properties. We do not attempt to model the change in integrated optical depth as a function of n, like Oonk et al. (2017) did, given that the number of free parameters is similar to the number of data points. Instead, we use the ratios between these lines. We will use the notation $R^{n}_{n'}$ to denominate the C$n\alpha$/C$n'\alpha$ line ratio, e.g., C357α/C539α line ratio will be R^{357}_{539}.

To generate R^{268}_{539}, R^{268}_{494} and R^{357}_{539} from the observations we use the respective velocity integrated optical depth maps (Figures 3.5 and 3.6). These line ratios are shown in Figure 3.7. In the case that one of the lines is not detected in one of the pixels we adopt the 3σ upper/lower limit on the integrated optical depth for the non detection. If two lines are not detected on a pixel we do not attempt to constrain the gas physical conditions. This limits our analysis for the -38 km s^{-1} velocity component to the western hotspot of Cas A, where the C268α line is detected (Figure 3.6).

The line ratios as a function of gas properties in the $n_{\rm e}$–$T_{\rm e}$ plane are shown in Figure 3.8 for three different locations in the map (see Figures 3.7 and 3.9). As a result of the C268α line being in emission and the C539α line in absorption R^{268}_{539} produces contours which have a similar shape to the constraint imposed by the transition from emission to absorption (Salgado et al., 2017b). The situation is similar for R^{268}_{494}. However intersecting the R^{357}_{539} constraint with either R^{268}_{539} or R^{268}_{494} restricts the range of allowed $n_{\rm e}$ and $T_{\rm e}$ values. The left panel of Figure 3.8 shows that the CRRL ratios used can constrain the gas properties in regions with high signal-to-noise ratio detections. Yet it also reveals that when one of the lines is not detected it is not possible to constrain the gas properties (e.g., right panel in Figure 3.8). In this case the line ratios constrain the gas electron density, and place a lower limit on the gas temperature. An upper limit on the gas temperature can be obtained if we consider the implied gas path length. If we restrict the models to path lengths smaller than 200 pc, this effectively puts an upper limit on the electron temperature of ≈ 160 K (Figure 3.8). We adopt an upper limit of 200 pc since we do not expect the gas structures to be larger than this in the line of sight direction.

Maps with the electron density, temperature and pressure constraints derived from the line ratio analysis for the -47 km s^{-1} velocity component are shown in Figure 3.9. The electron density shows almost no variation over the face of Cas A, while the electron temperature and pressure show a slight decrease towards the South. The electron density

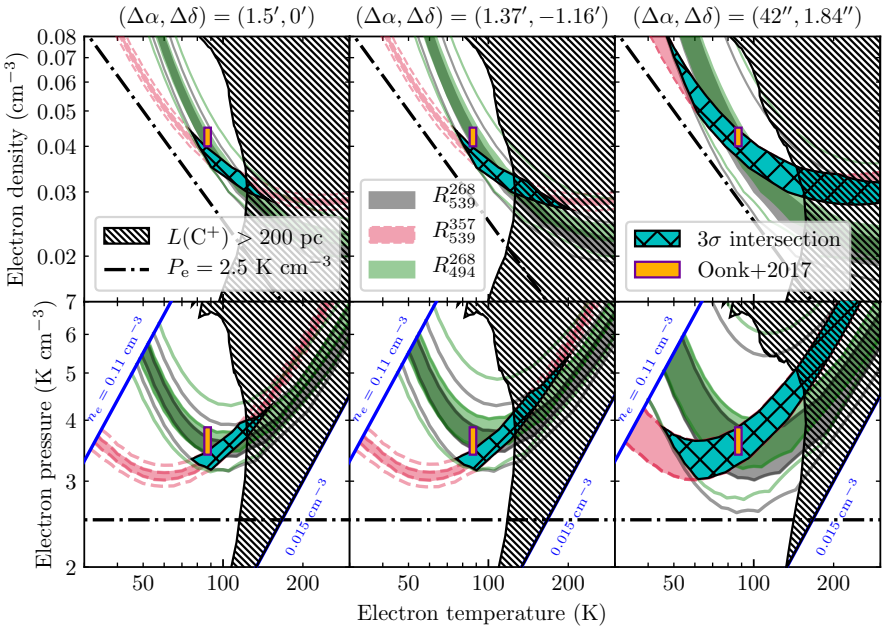

Figure 3.8.: Constraints imposed by the R^{268}_{539} =C268α/C539α, R^{357}_{539} =C357α/C539α and R^{268}_{494} =C268α/C494α line ratios in the n_e–T_e plane (*top panels*) and in the P_e–T_e plane (*bottom panels*). The constraints are shown for the −47 km s^{-1} velocity component at three different positions in the map. The positions, relative to the map centre, are shown on the top of the corresponding column. These positions are shown in Figures 3.7 and 3.9 as green crosses. The *orange rectangle with purple borders* shows the gas physical conditions derived by Oonk et al. (2017). The *dot-dashed line* shows a curve of constant electronic pressure. The *cyan region hatched with black lines* shows the intersection of the constraints imposed by the R^{268}_{539}, R^{357}_{539} and R^{268}_{494} line ratios if we consider their 3σ ranges. The *densely hatched region* shows where the required ionized carbon path length is larger than 200 pc. *Blue lines* in the bottom row show the limits of the grid of CRRL models.

has an almost constant value over the face of Cas A, however this largely due to the resolution of the model grid. In the density axis we have 18 resolution elements, while on the temperature axis we have 78 (Table 3.2). The discrete nature of the grid of models used to determine the electron temperature and density also results in abrupt changes in the gas properties. Additionally, this discreteness can produce patches which have sizes smaller than the spatial resolution of the data. This effect is particularly notorious in the T_e map (Figure 3.9).

As it is evident in Figure 3.8, we are constraining the gas properties to a given range. The size of this range will depend on the error bars of each pixel. For pixels with high signal-to-noise (left and centre panels in Figure 3.8) the uncertainty in electron density is about $\sim 30\%$ and in electron temperature $\sim 25\%$. While on pixels with lower signal to noise (right panel in Figure 3.8), the uncertainty can be of a factor of three or more. A change of about 25% in electron temperature translates into a 65% change in emission measure. In Table 3.3 we present the gas properties averaged over the face of Cas A. In this Table we provide the parameter ranges if we consider the 1σ uncertainties in the observed line ratios. In terms of the spatial distribution, this shows little change when we consider the uncertainties. The biggest change is on the mean value.

To estimate the hydrogen density from the electron density we assume that 94% and 100% of free electrons come from carbon for the -47 and -38 km s^{-1} velocity components respectively (Oonk et al., 2017). Additionally, we adopt a carbon abundance relative to hydrogen of 1.5×10^{-4} (Sofia et al., 1997). With this, the hydrogen density is 210–360 and 200–470 cm^{-3} for the -47 and -38 km s^{-1} velocity components respectively.

The largest uncertainty in the derived gas properties comes from the separation between the -47 and -38 km s^{-1} velocity components for the $n > 400$ lines. We test this effect by varying the integrated optical depth of the C539α line and comparing the derived values of n_e and T_e. We find that the electron temperature has an almost linear relation with the integrated optical depth of the C539α line, i.e. if we decrease the C539α line integrated optical depth by 30%, then the derived electron temperature decreases by 30%. For the electron density the change is less pronounced. A change of 30% in the integrated optical depth of the C539α line results in a change of less than 15% in the electron density.

Using the electron density and temperature maps and the C268α integrated optical depth we compute the ionized carbon emission measure, $EM_{\rm CII}$, column density, N(CII), and its path length along the line of sight, $L_{\rm CII}$. To determine the column density and $L_{\rm CII}$ we assume that 94% of the free electrons come from ionized carbon (Oonk et al., 2017). Maps with $EM_{\rm CII}$, N(CII) and $L_{\rm CII}$ for the -47 km s^{-1} velocity component are shown in Figure 3.10. These show a similar structure to the C268α integrated optical depth map, with larger values towards the South and West of Cas A. The structures smaller than the beam size are due to the strong dependence of the integrated optical depth on the electron temperature ($\propto T_e^{-5/2}$), and the discrete nature of the model grid used. For a constant electron and carbon density the only variation in the emission measure comes from variations in the path length of the gas along the line of sight. This will also be reflected in the column density $N(\mathrm{CII}) = L_{\rm CII} n_{\rm CII}$.

We compare the derived gas physical conditions against the spatially unresolved work

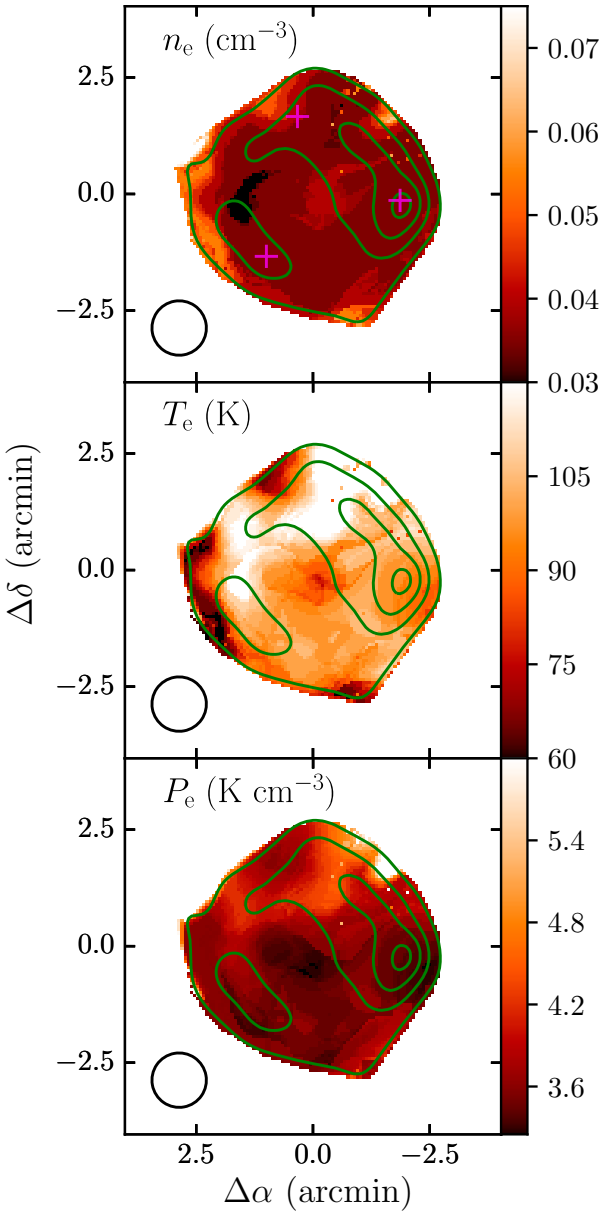

Figure 3.9.: Gas properties derived from the CRRL ratios for the Perseus arm component at −47 km s^{-1}. The *top panel* shows the electron density, the *middle panel* the electron temperature and the *bottom panel* the electron pressure. These are derived under the assumption of a constant radiation field of 1400 K at 100 MHz. The *pink crosses* in the top panel show the regions used in Figure 3.8. The 70″ resolution of these maps is shown in the bottom left corner of each map.

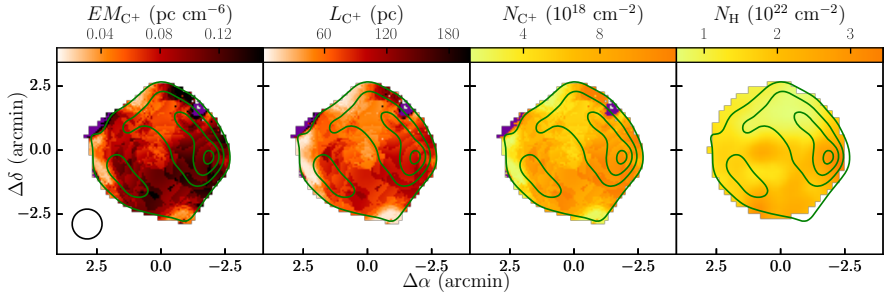

Figure 3.10.: C^+ emission measure EM_{CII}, path length L_{CII} and column density of ionized carbon N(CII) derived from the CRRL analysis for the Perseus arm component at −47 km s^{-1}, and the hydrogen column density map derived from the dust analysis by De Looze et al. (2017). The *leftmost column* shows the emission measure, the *middle left column* the path length, the *middle right column* the column density of ionized carbon and the *rightmost column* the hydrogen column density derived from analysis of the dust emission towards Cas A (De Looze et al., 2017). Regions where we cannot constrain the gas properties given the parameter space explored and observational uncertainties are shown with a colour not present in the colour bar. The 70″ resolution of these maps is shown in the bottom left corner of each map. The *green contours* show the 345 MHz continuum from Cas A at 51″ × 45″ resolution.

Table 3.3.: Ranges of the mean gas properties over the face of Cas A

Gas property	Velocity component	
	−47 km s^{-1}	−38 km s^{-1}
T_e (K)	71–137	50–145
n_e (cm^{-3})	0.03–0.055	0.03–0.07
P_e (K cm^{-3})	3.1–4.95	2.7–4.8
EM_{CII} (pc cm^{-6})	0.046–0.26	0.02–0.21
N_{CII} (10^{18} cm^{-2})	3.4–25.9	1.6–18.1
L_{CII} (pc)	27–182	10–180
n_H[a] (cm^{-3})	210–360	200–470
N_H[a] (10^{22} cm^{-2})	2.3–17.3	1–12
A_V[b]	11.5–360	200–470

[a] Assuming a carbon abundance relative to hydrogen of 1.5×10^{-4} (Sofia et al., 1997) and that 94% and 100% of the free electrons come from ionized carbon for the −47 and −38 km s^{-1} velocity components respectively (Oonk et al., 2017).

[b] Adopting $N_H = (2.08 \pm 0.02) \times 10^{21} A_V$ cm^{-2} (Zhu et al., 2017).

Table 3.4.: 158 μm-[CII] Line properties

Region	v_c (km s^{-1})	$\int I_\nu d\nu$ (10^{-5} erg cm^{-2} s^{-1} sr^{-1})	$L_{[CII]}$ ($L_\odot$)
1	-19 ± 15	6.70 ± 0.11	1.14 ± 0.02
2	-20 ± 15	5.99 ± 0.11	1.02 ± 0.02
3	-18 ± 15	6.15 ± 0.09	1.05 ± 0.01
4	-20 ± 15	6.76 ± 0.12	1.15 ± 0.02
5	-19 ± 15	4.65 ± 0.22	0.79 ± 0.04
6	-23 ± 15	5.10 ± 0.19	0.87 ± 0.03
7	-19 ± 15	6.92 ± 0.08	1.18 ± 0.01
8	-19 ± 15	6.74 ± 0.15	1.15 ± 0.02
9	-15 ± 15	7.14 ± 0.11	1.22 ± 0.02

of Oonk et al. (2017) towards the same background source to check for any differences. We focus on their study as it was the first one which was able to simultaneously explain the line width and integrated optical depth change with *n*. Additionally, this work and that of Oonk et al. (2017) use the same models, which reduces the need to account for different assumptions in the modelling. If we compare Table 3.3 with Table 7 of Oonk et al. (2017) we see that our results, averaged over the face of Cas A, are consistent.

3.3.5. 158 μm-[CII] LINE PROPERTIES

The 158 μm-[CII] line is the main coolant of the neutral diffuse ISM (e.g. Wolfire et al., 1995, 2003). Here we present the properties of the spatially resolved, velocity unresolved, 158 μm [CII] line.

To determine the properties of the 158 μm-[CII] line we fit a Gaussian profile to each of the nine PACS footprints. We only fit one Gaussian component since the line is unresolved in velocity. The best fit parameters of the Gaussian profile are presented in Table 3.4. These show little variation in the line frequency integrated intensity, but we do note that the lowest values are found in the northern footprints (5 and 6, see Figure 3.11). This could be due to the lower column densities found towards the north of Cas A (see Figure 3.10).

If we take the observed luminosity of the 158 μm-[CII] line and compare it to the CRRL derived gas column density we obtain values of the order of $(1.4 \pm 0.1) \times 10^{-26}$ erg s^{-1} (H-atom)$^{-1}$. This cooling [CII] rate is is somewhat less than the cooling rate derived from ultraviolet absorption line studies originating from the upper fine structure level in sighlines through nearby diffuse clouds ($(3–10) \times 10^{-26}$ erg s^{-1} (H-atom)$^{-1}$ Pottasch et al., 1979; Gry et al., 1992) but comparable to the average cooling rate of the Galaxy, $(2.65 \pm 0.15) \times 10^{-26}$ erg s^{-1} (H-atom)$^{-1}$ (Bennett et al., 1994). For the CRRL derived column densities (Table 3.3), the 158 μm-[CII] line will be optically thick (e.g., Tielens & Hollenbach, 1985). If the [CII] line is optically thick, then the observed line does not account for the total line of sight ionized carbon column which

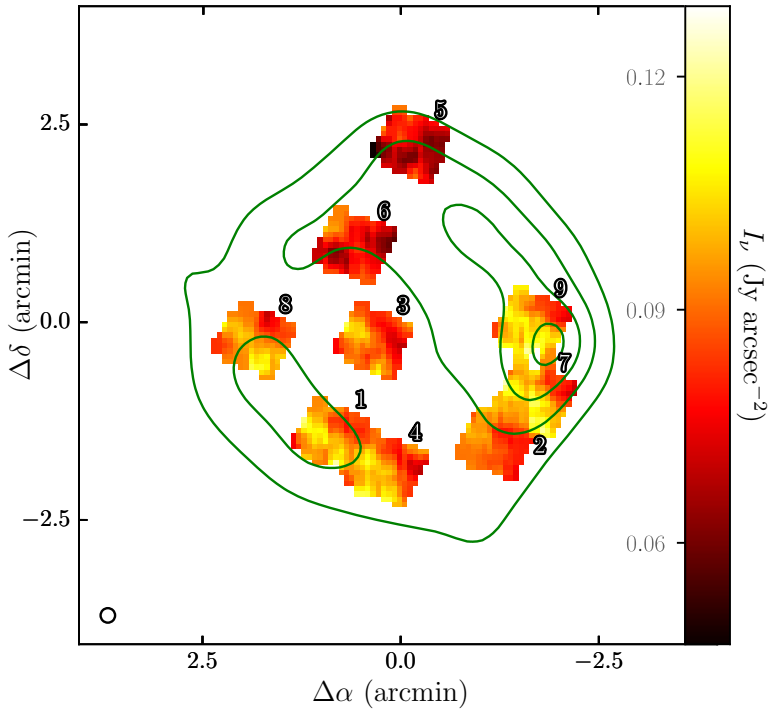

Figure 3.11.: Map of 158 μm-[CII] line emission obtained with Herschel PACS. In these the [CII] line is unresolved in velocity, and only $\sim$ 20% of the surface of Cas A is covered. This map is shown at its native resolution of 12″.

in turn results in a lower [CII] cooling rate.

3.4. Discussion

3.4.1. Comparison with other tracers

We compare the CRRL optical depth with lines which trace different components of the ISM. These include diffuse atomic gas (21 cm-HI, Bieging et al., 1991), diffuse molecular gas (18 cm-OH, Bieging & Crutcher, 1986), translucent gas (492 GHz–[CI], Mookerjea et al., 2006) and dense molecular gas (CO, Wilson et al., 1993; Liszt & Lucas, 1999; Kilpatrick et al., 2014).

Spatial distribution

A comparison between the optical depths of 21 cm-HI, C268α and the ^{12}CO(2–1) line is presented in Figure 3.12. This shows that most of the C268α emission comes from regions where HI is saturated (cyan pixels in the HI maps). The ^{12}CO(2–1) line also shows structures which are well correlated with the ones seen in C268α and 21 cm-HI. However, the peaks of CO emission are generally located outside the face of Cas A, which does not allow for a direct comparison. One exception is at a velocity of -47.8 km s^{-1}, where a peak of ^{12}CO(2–1) emission is located over the face of Cas A. In this case the distance between the peaks of ^{12}CO(2–1) and C268α is $87''$.

The spatial distribution of ^{12}CO(2–1) shows that most of the gas at -41 km s^{-1} is located to the West of Cas A, while the gas at -36.5 km s^{-1} extends from the west to the south east of Cas A (Kilpatrick et al., 2014). Both velocity components overlap towards the West of Cas A. This makes the distinction of these velocity components more difficult in this region.

To explore the relation between CO emission and CRRL emission we draw a slice joining the peaks of ^{12}CO(2–1) and C268α emission at a velocity of -47.8 km s^{-1}. The slice is shown as a green line in Figure 3.12 in the panels with a velocity of -47.8 km s^{-1}. The normalised intensity or optical depth of different tracers along this slice is shown in Figure 3.13. Here we notice how the optical depth of C268α and Cα(537) peaks at the same location, and the molecular lines peak towards the left of the CRRLs, which corresponds to the South-East direction in the sky. The difference between the peaks of the CRRLs and the molecular lines is similar to that expected in a photo-dissociation region (PDR, e.g., Hollenbach & Tielens, 1999). As we move towards the South-East of Cas A the gas shows a CII/CI/CO layered structure, which suggests that we are observing the photodissociation region associated with the edge of a molecular cloud.

The distance at which the gas becomes CO bright will depend on the average PDR density. The projected distance on the plane of the sky between the peak of the C268α optical depth and the peak of the ^{12}CO(2–1) emission is $1.3 \pm 0.6'$. If we assume that the Perseus arm gas is at a distance of 3.16 ± 0.02 kpc from Earth in the direction of Cas A (Choi et al., 2014; Salas et al., 2017), then this corresponds to $\sim 1.2 \pm 0.5$ pc in the plane of the sky. CO will be sufficiently shielded from photo-dissociating photons when $A_{\rm FUV} \sim 1$. We adopt a conversion factor between extinction in the V band

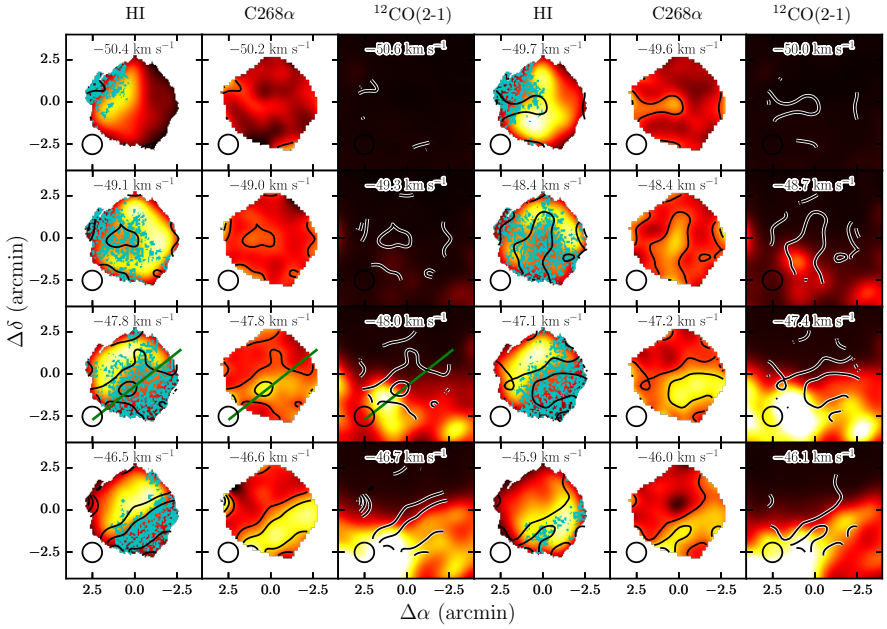

Figure 3.12.: Comparison between the optical depths of 21 cm-HI, C268α and the ^{12}CO(2–1) line brightness. Masked pixels in the 21 cm-HI optical depth maps are shown in cyan. The *green line* in the −47.8 km s^{-1} map shows the slice used to study the gas between the peaks of the ^{12}CO(2–1) and C268α lines. The 70″ resolution of these maps is shown in the bottom left corner of each map.

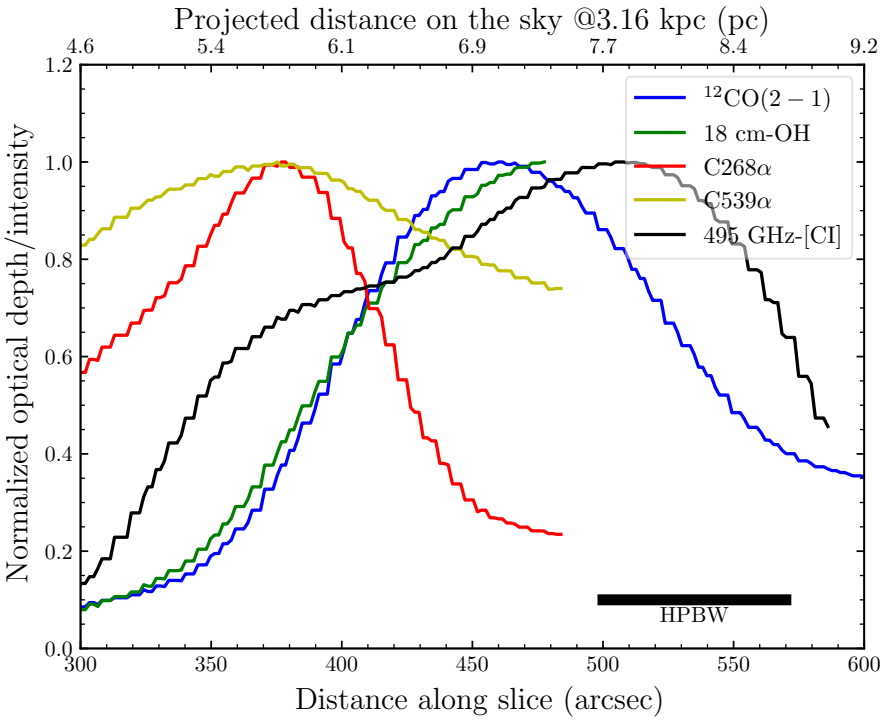

Figure 3.13.: Comparison between different ISM tracers along a slice joining the C268α optical depth peak and ^{12}CO(2–1) line peak at a velocity of −47.8 km s^{-1}. The *black bar* at the bottom shows the half power beam width (70″) of the images. The *top axis* shows the plane of the sky distance along the slice assuming that the gas is at a distance of 3.16 kpc from the observer (Salas et al., 2017). Given that the gas could be closer to the observer this distance is an upper limit.

and hydrogen column density of $N_{\rm H} = (2.08 \pm 0.02) \times 10^{21} A_{\rm V}$ cm^{-2} (Zhu et al., 2017). Then, to convert between optical opacity and far-ultra violet (FUV) opacity we adopt $\kappa_{\rm d}({\rm FUV}) \approx 1.8\kappa_{\rm d}({\rm V})$. With this, for an $A_{\rm FUV}$ of one magnitude we have $N_{\rm H} = (1.15 \pm 0.01) \times 10^{21}$ cm^{-2}. This implies that the mean density in this PDR is $n_{\rm H} = 310 \pm 28$ cm^{-3}. This density is consistent with the hydrogen density derived from the CRRL analysis (Table 3.3).

Motivated by the observed layered structure we compare the CO emission to that of an edge-on PDR model. This model is an extension of the Tielens & Hollenbach (1985) PDR model which includes the updates of Wolfire et al. (2010) and Hollenbach et al. (2012). The calculation of line intensities and source parameters for edge-on models are discussed in Pabst et al. (2017). We use a total hydrogen density of 300 cm^{-3}, an $A_{\rm V}$ of eight along the line of sight and of eight in the transverse direction. The gas in the PDR is illuminated on one side by an interstellar radiation field with $G_0 = 4.2$, measured in Habing (1968) units, and primary cosmic ray ionisation rate per hydrogen

of 7×10^{-17} s^{-1}. The carbon and hydrogen RRLs observed towards Cas A (Oonk et al., 2017) have been reanalysed by Neufeld et al. (subm) taking into account the relevant chemical recombination routes and we have adopted values of the radiation field and cosmic-ray ionisation rate consistent with their results. We adopt an abundance ^{12}CO/^{13}CO of 60, appropriate for gas in the Perseus arm in this direction (Langer & Penzias, 1990; Milam et al., 2005).

The comparison between observations and the output from the PDR model is presented in Figure 3.14. The adopted density ensures that the calculated distance on the sky between the CO peak and the surface of the PDR, as defined by the CRRL peak, agrees with the observations. For $A_V \geq 0.5$ the increase in the line intensity is well described by the model. For $A_V \sim 0.9$ the proximity to the edge of the mapped region causes the velocity integrated line intensity to decrease. This decrease close to the map edge is caused by the convolution with a $70''$ beam.

Additionally, we use the same model to predict the velocity integrated line intensity of the 492 GHz-[CI] and 158 μm-[CII] lines, and the optical depth of the 18 cm-OH line. The model does a good job in reproducing the observed optical depth of the OH line. In the region where the slice intersects footprint 1 of the PACS 158 μm-[CII] cube (Figure 3.11), the model predicts a value of 4.3×10^{-5} erg cm^{-2} s^{-1} sr^{-1}. The observed value is 56% larger, which can be accounted for by the prescence of gas at higher velocities not present in the model (e.g., the -38 and 0 km s^{-1} velocity components present in the velocity unresolved PACS observations). However, in the case of atomic carbon, the model overestimates the observed values by a factor of five. This is similar to that found in other lines of sight, where the predicted atomic carbon column density is larger than the observed one (e.g., Gong et al., 2017).

De Looze et al. (2017) find an interstellar radiation field (ISRF) with a strength $G_0 \sim 0.6$. This value is lower than the one adopted here, but we do note that against Cas A it is not possible to use the dust spectral energy distribution to estimate the strength of the ISRF. Outside the area covered by Cas A De Looze et al. (2017) find strengths for the ISRF of the order of unity. However, the derived strength of the ISRF will depend on the adopted model with a variation of up to 1.6 depending on the model details (e.g., Fanciullo et al., 2015; Planck Collaboration et al., 2016). In their work De Looze et al. (2017) also use line ratios and the PDR toolbox models (Pound & Wolfire, 2008) to estimate the strength of the ISRF in the ISM between Cas A and Earth. They find that the line ratios are consistent with their dust derived value of $G_0 \sim 0.6$, but the line ratio is also consistent with a lower density and stronger ISRF (see Figure C1 in De Looze et al., 2017). Based on the current data we infer that the adopted value is in reasonable agreement with all observations.

GAS COLUMN DENSITY

For the -47 km s^{-1} feature most of the 21 cm-HI optical depth maps show that the line is saturated with values of $\tau \gtrsim 5$ (Bieging et al., 1991). Nonetheless, this lower limit on the optical depth can be used to place a lower limit on the atomic hydrogen column density. If we assume that the width of the 21 cm-HI line profile at -47 km s^{-1} is the same as that of the CRRL at the same velocity, and that the spin temperature is

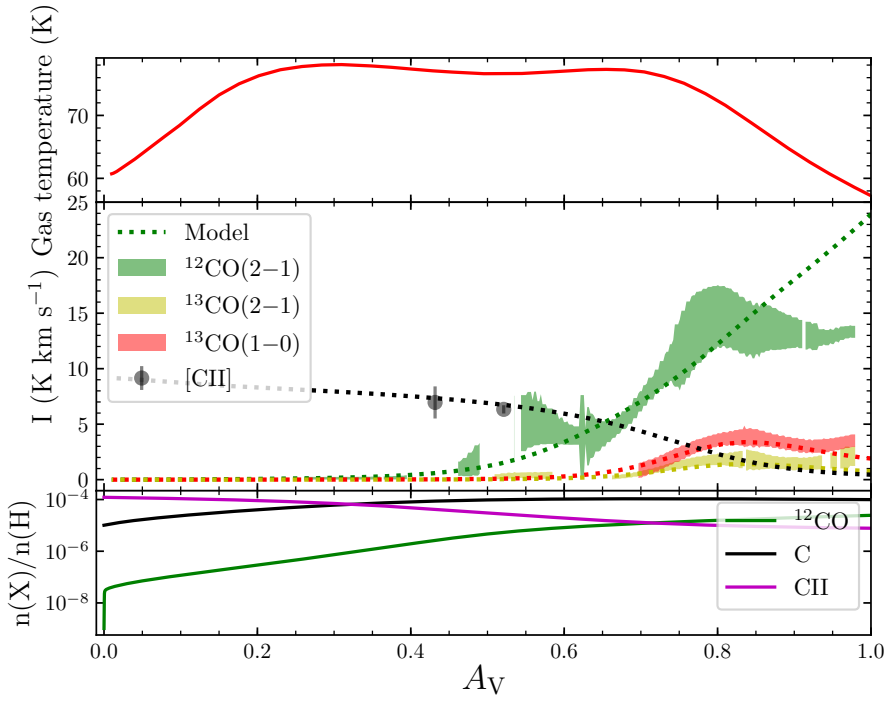

Figure 3.14.: Comparison between the ^{12}CO(2–1), ^{13}CO(1–0), ^{13}CO(2–1) and 158 μm [CII] velocity integrated line intensity along the slice shown in Figure 3.13. The observed quantities (*shaded regions*) are compared with a PDR model (*dashed lines*). The *shaded regions* show the observed values and their 3σ error range. The 158 μm [CII] points have been rescaled to be visible in this Figure. The PDR model is that of a region with a constant hydrogen density of 300 cm^{-3}, an incident radiation field of $G_0 = 4.2$ on one side of the cloud, and a line of sight optical interstellar extinction of eight. For more details on the PDR model see the text and Pabst et al. (2017).

greater than 50 K, then we have that $N(\mathrm{HI}) > 1.5 \times 10^{21}$ cm^{-2}. This limit is consistent with the column density derived from the CRRL and edge-on PDR analysis and it implies a fraction $N(\mathrm{HI})/N(\mathrm{H_2}) \gtrsim 0.1$.

Additional estimates of the gas column density can be obtained from measurements of X-ray absorption and from the dust optical depth. In the case of X-ray absorption Hwang & Laming (2012) determined values of 2×10^{22} cm^{-2} over the South portion of Cas A, with higher values ($\sim 3 \times 10^{22}$ cm^{-2}) towards its western hotspot. These values are slightly smaller than the ones found using the CRRLs lines. We consider that this difference is not significant given the uncertainties associated with X-ray column density measurements (e.g., Predehl & Schmitt, 1995; Zhu et al., 2017). Recently, De Looze et al. (2017) modelled the dust emission towards Cas A and used it to determine the mass of dust in the ISM along the line of sight. They adopted a dust-to-gas ratio of 0.0056 and found column densities of 1.5×10^{22} cm^{-2} towards the south of Cas A, and 2.2×10^{22} cm^{-2} towards the western hotspot. A map showing the spatial distribution of column density derived from the dust analysis is shown in the rightmost panel of Figure 3.10. A comparison between the column densities derived from the dust and CRRL analysis (right panels in Figure 3.10) shows good agreement, with larger values towards the South of Cas A and a peak against its western hotspot. To compare their magnitudes we focus on regions towards the South of the centre of Cas A, where we see less emission from gas at -38 km s^{-1} which would create confusion. Here the magnitude of the CRRL derived gas column density, (2.4–11.3 $\times 10^{22}$ cm^{-2}, is comparable to that derived from the dust analysis. The major uncertainty in the determination of the ISM dust content along this line of sight comes from the separation between the foreground ISM dust component and the contribution from dust associated with the supernova remnant. This introduces a factor of a few uncertainty in the derived dust mass and column density.

The CRRL derived gas column density averaged over the face of Cas A, (3.4–25.9) $\times$ 10^{18} cm^{-2}, on its own implies an hydrogen column density of (2.3–17.3) $\times 10^{22}$ cm^{-2}. Given that not all of the carbon is ionized, we also need to account for carbon in atomic and molecular forms. We focus on a region to the South of the center of Cas A, following the slice in Figure 3.12, where there is CO emission. Here, with an adopted A_V of eight, our PDR model is able to reproduce the CO observations. However, for an A_V of eight and an excitation temperature $\sim$ 20 K, the CO lines used here are optically thick. This points towards the presence of denser CO-rich clumps embedded in a lower density CO-dark halo. This situation is similar to that observed towards the W43 star forming region, where large column densities are derived from atomic hydrogen observations at 21 cm ($N_\mathrm{H} \approx 2 \times 10^{22}$ cm^{-2}, Bihr et al., 2015; Bialy et al., 2017). Gamma-ray and dust observations in our Galaxy have revealed the prescence of large reservoirs of CO-dark molecular gas (with a mass fraction comparable to that of the CO molecular gas Grenier et al., 2005; Planck Collaboration et al., 2011). Likely, much of this gas is in extended atomic hydrogen halos around giant molecular cloud complexes in spiral arms such as the ones probed in this study in the Perseus arm.

3.4.2. Envelopes of molecular clouds

The gas properties derived from the CRRL analysis seem to bridge the gap between the atomic gas traced by the 21 cm line of HI and the molecular gas traced by the CO lines in the millimimeter (Oonk et al., 2017; Salas et al., 2017). From spatially unresolved observations of the 21 cm-HI line in this direction Davies & Matthews (1972) derived a temperature of 140 ± 40 K for the two most prominent Perseus arm absorption features at -47 and -38 km s^{-1}. It has not been possible to estimate this value on smaller scales due to the saturation of the 21 cm-HI line at these velocities (e.g., Bieging et al., 1991), but it is likely to be slightly colder. On the molecular side of things we have temperatures of $\sim$ 20 K (Batrla et al., 1984). This would put the gas traced by low frequency CRRLs, with an electron temperature of $\sim$ 80 K, in between atomic and molecular gas. A place where this transition takes place is the envelope of molecular clouds (e.g., Moriarty-Schieven et al., 1997; Krumholz et al., 2009; Sternberg et al., 2014).

Studies of molecular clouds in the solar vicinity show that their atomic envelopes have temperatures of the order $\sim$ 100 K (Andersson et al., 1991). A comparisson between gas traced by the 21 cm HI and the ^{13}CO lines shows that the atomic component is more extended than the molecular one and their velocity fields are not necessarily aligned (Imara & Blitz, 2011). The properties of the envelope will depend on the environment. Here we compare against two giant molecular clouds, both show large fractions of atomic gas, but one shows little star formation, with an infrared luminosity of $\approx$ 5000 L$_\odot$; G216–2.5 (the Maddalena-Thaddeus cloud, Maddalena & Thaddeus, 1985; Williams & Maddalena, 1996; Megeath et al., 2009; Imara, 2015) and the other a mini-starburst with an infrared luminosity of 3.5×10^6 L$_\odot$ (Motte et al., 2003; Nguyen Luong et al., 2011; Bihr et al., 2015; Bialy et al., 2017). The atomic envelope around G216–2.5 has a thickness of $\sim$ 50 pc and the atomic gas column density inferred from observations of the 21 cm line of HI is $\approx 2.21 \times 10^{21}$ cm^{-2} (Williams & Maddalena, 1996). Around W43, the atomic envelope has a thickness of 140 pc (Motte et al., 2014), and the atomic gas column density is $\approx 2 \times 10^{22}$ cm^{-2} (Bihr et al., 2015; Bialy et al., 2017). The later column density is consistent with the lower end of the ranges found here (Table 3.3).

Another way in which we can study the envelopes of giant molecular clouds is with observations of the 158 μm-[CII] line. In cases where it is possible to isolate an ionized carbon layer around a molecular cloud it is found that the gas temperature and density are close to those found here. In the Magellanic clouds Pineda et al. (2017) find densities of 700–2000 cm^{-3} and temperatures of $\sim$ 50 K.

3.4.3. Uncertainties in the CRRL modelling

The change in line properties as a function of physical properties is quite sensitive to the gas physical conditions. During the modelling of the CRRL line properties as a function of principal quantum number a series of assumptions are made which have an effect on the derived gas properties. Some of these have been explored previously, like the use of different angular momentum changing collisional rates (Salgado et al., 2017a),

or including collisions with hydrogen when solving the level population problem (Oonk et al., 2017). Additionally, two assumptions have not been explored before, those are; the use of different collisional rates for the excitation of ionized Carbon and changing the carbon and electron abundances relative to hydrogen. Having different collisional rates and abundances will change the dielectronic capture rate. This will be reflected as a change in the departure coefficient b_n, which determines how the integrated optical depth will behave as a function of n.

Given that it is computationally expensive to recompute the grid of models for each set of assumptions, we focus on a particular point in the $n_{\rm e} - T_{\rm e}$ plane. The change in the $b_n\beta_{n,n'}$ coefficients as a function of n is shown in Figure 3.15 for different assumptions. These show that the change in the integrated optical depth will be $\sim 10\%$ for the models computed using the different collisional rates and lower carbon and electron abundances. For other assumptions the difference will be lower.

Recently, Guzmán et al. (2017) and Vrinceanu et al. (2017) have investigated the effect of using different formulations (semi-classical versus quantum mechanical) when computing the ℓ-changing collisional rates. As shown by Salgado et al. (2017a, See their Figure 14) this will affect the departure coefficients, mainly their absolute values. However, as Guzmán et al. (2017) and Vrinceanu et al. (2017) point out, there is no physical reason to prefer one formulation over the other. A more detailed comparison of the effect different formulations will have on the predicted CRRL properties will be investigated in the future.

3.5. SUMMARY

We have presented $70''$ resolution CRRL maps at 340, 148, 54 and 43 MHz. The distribution of the C268α line in emission reveals a good correlation with regions where the 21 cm-HI line is saturated and regions of faint ^{12}CO(2–1) emission. We interpret this as as a diffuse PDR, in which low frequency CRRLs trace the less dense, warmer envelope of molecular gas.

Using the ratios between CRRLs we have constrained the gas electron temperature and density along the line of sight on scales of $\lesssim 1.2$ pc. With the line ratios used here, the constraints result in a range of allowed electron temperatures and densities. Averaged over the face of Cas A the constraints on the electron density are $n_{\rm e} = (0.03\text{–}0.055)$ cm^{-3} and $T_{\rm e} =$ (70–140 K for gas in the Perseus arm of the Galaxy at -47 km s^{-1}. The pressure shows variations of less than a factor of two on $\lesssim 1.2$ pc scales.

From the constraints on the electron temperature and density we derived lower limits for the ionized carbon emission measure, column density and its line of sight path length. The lower limit on the column density is 3.4×10^{18} cm^{-2}, which corresponds to an hydrogen column density of 2.2×10^{22} cm^{-2} if all carbon is ionized and [C/H]= 1.5×10^{-4}. The hydrogen density derived from analysis of the CRRLs integrated optical depths is 210–360 cm^{-3}.

A PDR model with an average hydrogen density of 300 cm^{-3}, and conditions similar to those inferred for the clouds in this region, is able to reproduce the observed distribution of ^{12}CO(2–1), ^{13}CO(2–1), ^{13}CO(1–0) and 1667 MHz OH.

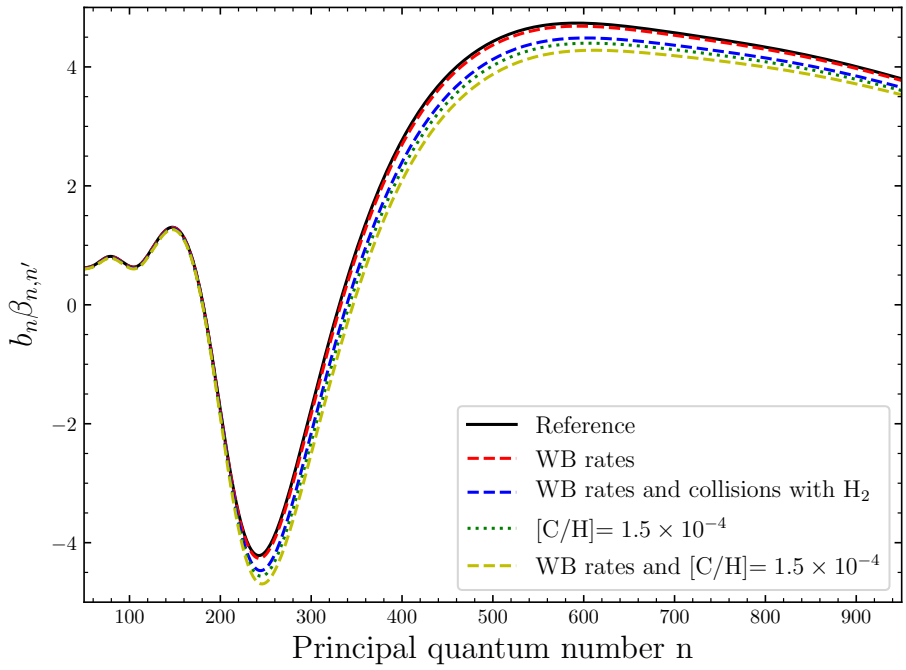

Figure 3.15.: Comparison between CRRL models under different assumptions regarding the carbon ion collisional excitation rates, carbon and electron abundances. All models were computed for an electron density of 0.05 cm^{-3} and temperature 80 K. The reference model is one computed assuming $[C/H] = [e/H] = 3 \times 10^{-4}$ and using the Tielens & Hollenbach (1985) and Hayes & Nussbaumer (1984) collisional rates. The models labelled with WB rates use the Wilson & Bell (2002) rates for collisions with electrons and those of Barinovs et al. (2005) for collisions with atomic hydrogen. The model which includes collisions with molecular hydrogen, H_2, uses the rate for collisions with molecular hydrogen presented in Goldsmith et al. (2012). The models labelled with $[C/H] = 1.5 \times 10^{-4}$ use this abundance for carbon and electrons. The largest difference for and individual change is produced when the electron and carbon abundances are modified.

The relatively high spatial resolution of the present observations enables us to study the relation between CRRLs and other tracers of the ISM on scales where it is possible to observe the PDR like structure in the surface of a molecular cloud. This also highlights the importance of CRRLs as tracers of the diffuse ISM, as they allow us to determine the gas physical conditions in regions which are not readily traced by 21 cm-HI and/or CO. These observations highlight the utility of CRRLs as tracers of low density extended HI and CO-dark gas halo's around molecular clouds. Future surveys of CRRLs with the low frequency array (LOFAR) are promising as they could reveal important new clues about the physics of the ISM, particularly about the transition from atomic-to-molecular gas and the properties of CO-dark gas.

BIBLIOGRAPHY

Anantharamaiah, K. R., Erickson, W. C., Payne, H. E., & Kantharia, N. G. 1994, ApJ, 430, 682

Anantharamaiah, K. R., Payne, H. E., & Erickson, W. C. 1988, MNRAS, 235, 151

Andersson, B.-G., Wannier, P. G., & Morris, M. 1991, ApJ, 366, 464

Asgekar, A., Oonk, J. B. R., Yatawatta, S., et al. 2013, A&A, 551, L11

Astropy Collaboration, Robitaille, T. P., Tollerud, E. J., et al. 2013, A&A, 558, A33

Barinovs, Ğ., van Hemert, M. C., Krems, R., & Dalgarno, A. 2005, ApJ, 620, 537

Batrla, W., Walmsley, C. M., & Wilson, T. L. 1984, A&A, 136, 127

Bennett, C. L., Fixsen, D. J., Hinshaw, G., et al. 1994, ApJ, 434, 587

Bialy, S., Bihr, S., Beuther, H., Henning, T., & Sternberg, A. 2017, ApJ, 835, 126

Bieging, J. H., & Crutcher, R. M. 1986, ApJ, 310, 853

Bieging, J. H., Goss, W. M., & Wilcots, E. M. 1991, ApJS, 75, 999

Bihr, S., Beuther, H., Ott, J., et al. 2015, A&A, 580, A112

Blitz, L., & Williams, J. P. 1999, in NATO Advanced Science Institutes (ASI) Series C, Vol. 540, NATO Advanced Science Institutes (ASI) Series C, ed. C. J. Lada & N. D. Kylafis, 3

Briggs, D. S. 1995, in Bulletin of the American Astronomical Society, Vol. 27, American Astronomical Society Meeting Abstracts, 1444

Cazaux, S., & Tielens, A. G. G. M. 2004, ApJ, 604, 222

Choi, Y. K., Hachisuka, K., Reid, M. J., et al. 2014, ApJ, 790, 99

Dame, T. M. 2011, ArXiv e-prints

Davies, R. D., & Matthews, H. E. 1972, MNRAS, 156, 253

De Looze, I., Barlow, M. J., Swinyard, B. M., et al. 2017, MNRAS, 465, 3309

de Oliveira-Costa, A., Tegmark, M., Gaensler, B. M., et al. 2008, MNRAS, 388, 247

Dickey, J. M., Strasser, S., Gaensler, B. M., et al. 2009, ApJ, 693, 1250

Erickson, W. C., McConnell, D., & Anantharamaiah, K. R. 1995, ApJ, 454, 125

Ershov, A. A., Lekht, E. E., Smirnov, G. T., & Sorochenko, R. L. 1987, Soviet Astronomy Letters, 13, 8
Fanciullo, L., Guillet, V., Aniano, G., et al. 2015, A&A, 580, A136
Fukui, Y., Kawamura, A., Wong, T., et al. 2009, ApJ, 705, 144
Gibson, S. J. 2002, in Astronomical Society of the Pacific Conference Series, Vol. 276, Seeing Through the Dust: The Detection of HI and the Exploration of the ISM in Galaxies, ed. A. R. Taylor, T. L. Landecker, & A. G. Willis, 235
Goldsmith, P. F., Langer, W. D., Pineda, J. L., & Velusamy, T. 2012, ApJS, 203, 13
Gong, M., Ostriker, E. C., & Wolfire, M. G. 2017, ApJ, 843, 38
Gordon, M. A., & Sorochenko, R. L., eds. 2009, Astrophysics and Space Science Library, Vol. 282, Radio Recombination Lines
Grenier, I. A., Casandjian, J.-M., & Terrier, R. 2005, Science, 307, 1292
Gry, C., Lequeux, J., & Boulanger, F. 1992, A&A, 266, 457
Guzmán, F., Badnell, N. R., Williams, R. J. R., et al. 2017, MNRAS, 464, 312
Habing, H. J. 1968, BAN, 19, 421
Hayes, M. A., & Nussbaumer, H. 1984, A&A, 134, 193
Hollenbach, D., Kaufman, M. J., Neufeld, D., Wolfire, M., & Goicoechea, J. R. 2012, ApJ, 754, 105
Hollenbach, D. J., & Tielens, A. G. G. M. 1999, Reviews of Modern Physics, 71, 173
Hwang, U., & Laming, J. M. 2012, ApJ, 746, 130
Imara, N. 2015, ApJ, 803, 38
Imara, N., & Blitz, L. 2011, ApJ, 732, 78
Kantharia, N. G., & Anantharamaiah, K. R. 2001, Journal of Astrophysics and Astronomy, 22, 51
Kantharia, N. G., Anantharamaiah, K. R., & Payne, H. E. 1998, ApJ, 506, 758
Kavars, D. W., Dickey, J. M., McClure-Griffiths, N. M., Gaensler, B. M., & Green, A. J. 2003, ApJ, 598, 1048
—. 2005, ApJ, 626, 887
Kerton, C. R. 2005, ApJ, 623, 235
Kilpatrick, C. D., Bieging, J. H., & Rieke, G. H. 2014, ApJ, 796, 144
Konovalenko, A. A. 1984, Soviet Astronomy Letters, 10, 353
Krumholz, M. R., McKee, C. F., & Tumlinson, J. 2009, ApJ, 693, 216
Langer, W. D., & Penzias, A. A. 1990, ApJ, 357, 477
Liszt, H., & Lucas, R. 1999, A&A, 347, 258
Maddalena, R. J., & Thaddeus, P. 1985, ApJ, 294, 231
McMullin, J. P., Waters, B., Schiebel, D., Young, W., & Golap, K. 2007, in Astronomical Society of the Pacific Conference Series, Vol. 376, Astronomical Data Analysis Software and Systems XVI, ed. R. A. Shaw, F. Hill, & D. J. Bell, 127
Mebold, U., & Hills, D. L. 1975, A&A, 42, 187
Megeath, S. T., Allgaier, E., Young, E., et al. 2009, AJ, 137, 4072
Milam, S. N., Savage, C., Brewster, M. A., Ziurys, L. M., & Wyckoff, S. 2005, ApJ, 634, 1126
Mookerjea, B., Kantharia, N. G., Roshi, D. A., & Masur, M. 2006, MNRAS, 371, 761
Moriarty-Schieven, G. H., Wannier, & P. G. 1997, ApJ, 475, 642

Moss, V. A., McClure-Griffiths, N. M., Braun, R., Hill, A. S., & Madsen, G. J. 2012, MNRAS, 421, 3159
Motte, F., Schilke, P., & Lis, D. C. 2003, ApJ, 582, 277
Motte, F., Nguyên Luong, Q., Schneider, N., et al. 2014, A&A, 571, A32
Neufeld, D. A., Wolfire, M. G., Oonk, J. B. R., Tielens, A. G. G. M., & Salas, P. subm, submitted
Nguyen Luong, Q., Motte, F., Schuller, F., et al. 2011, A&A, 529, A41
Oonk, J. B. R., van Weeren, R. J., Salas, P., et al. 2017, MNRAS, 465, 1066
Oonk, J. B. R., van Weeren, R. J., Salgado, F., et al. 2014, MNRAS, 437, 3506
Pabst, C. H. M., Goicoechea, J. R., Teyssier, D., et al. 2017, A&A, 606, A29
Pascucci, I., Edwards, S., Heyer, M., et al. 2015, ApJ, 814, 14
Payne, H. E., Anantharamaiah, K. R., & Erickson, W. C. 1989, ApJ, 341, 890
—. 1994, ApJ, 430, 690
Pineda, J. L., Langer, W. D., Goldsmith, P. F., et al. 2017, ApJ, 839, 107
Planck Collaboration, Ade, P. A. R., Aghanim, N., et al. 2011, A&A, 536, A19
—. 2016, A&A, 586, A132
Pottasch, S. R., Wesselius, P. R., & van Duinen, R. J. 1979, A&A, 74, L15
Pound, M. W., & Wolfire, M. G. 2008, in Astronomical Society of the Pacific Conference Series, Vol. 394, Astronomical Data Analysis Software and Systems XVII, ed. R. W. Argyle, P. S. Bunclark, & J. R. Lewis, 654
Predehl, P., & Schmitt, J. H. M. M. 1995, A&A, 293, 889
Reed, J. E., Hester, J. J., Fabian, A. C., & Winkler, P. F. 1995, ApJ, 440, 706
Roshi, D. A., & Kantharia, N. G. 2011, MNRAS, 414, 519
Roshi, D. A., Kantharia, N. G., & Anantharamaiah, K. R. 2002, A&A, 391, 1097
Salas, P., Oonk, J. B. R., van Weeren, R. J., et al. 2017, MNRAS, 467, 2274
Salgado, F., Morabito, L. K., Oonk, J. B. R., et al. 2017a, ApJ, 837, 141
—. 2017b, ApJ, 837, 142
Schwarz, U. J., Goss, W. M., & Kalberla, P. M. W. 1997, A&AS, 123
Shaver, P. A. 1975, Pramana, 5, 1
Sofia, U. J., Cardelli, J. A., Guerin, K. P., & Meyer, D. M. 1997, ApJL, 482, L105
Sorochenko, R. L., & Smirnov, G. T. 2010, Astronomy Reports, 54, 776
Sorochenko, R. L., & Walmsley, C. M. 1991, Astronomical and Astrophysical Transactions, 1, 31
Stanimirović, S., Murray, C. E., Lee, M.-Y., Heiles, C., & Miller, J. 2014, ApJ, 793, 132
Stepkin, S. V., Konovalenko, A. A., Kantharia, N. G., & Udaya Shankar, N. 2007, MNRAS, 374, 852
Sternberg, A., Le Petit, F., Roueff, E., & Le Bourlot, J. 2014, ApJ, 790, 10
Tielens, A. G. G. M., & Hollenbach, D. 1985, ApJ, 291, 722
Troland, T. H., Crutcher, R. M., & Heiles, C. 1985, ApJ, 298, 808
van Gorkom, J. H., & Ekers, R. D. 1989, in Astronomical Society of the Pacific Conference Series, Vol. 6, Synthesis Imaging in Radio Astronomy, ed. R. A. Perley, F. R. Schwab, & A. H. Bridle, 341
van Haarlem, M. P., Wise, M. W., Gunst, A. W., et al. 2013, A&A, 556, A2
van Langevelde, H. J., & Cotton, W. D. 1990, A&A, 239, L5
Vrinceanu, D., Onofrio, R., & Sadeghpour, H. R. 2012, ApJ, 747, 56

—. 2017, MNRAS, 471, 3051
Watson, W. D., Western, L. R., & Christensen, R. B. 1980, ApJ, 240, 956
Williams, J. P., & Maddalena, R. J. 1996, ApJ, 464, 247
Wilson, N. J., & Bell, K. L. 2002, MNRAS, 337, 1027
Wilson, T. L., Mauersberger, R., Muders, D., Przewodnik, A., & Olano, C. A. 1993, A&A, 280, 221
Wolfire, M. G., Hollenbach, D., & McKee, C. F. 2010, ApJ, 716, 1191
Wolfire, M. G., Hollenbach, D., McKee, C. F., Tielens, A. G. G. M., & Bakes, E. L. O. 1995, ApJ, 443, 152
Wolfire, M. G., McKee, C. F., Hollenbach, D., & Tielens, A. G. G. M. 2003, ApJ, 587, 278
Xu, Y., Reid, M. J., Zheng, X. W., & Menten, K. M. 2006, Science, 311, 54
Zheng, H., Tegmark, M., Dillon, J., et al. 2016, ArXiv e-prints
Zhu, H., Tian, W., Li, A., & Zhang, M. 2017, MNRAS, 471, 3494